

PART 3

INFRARED PERSPECTIVES ON ATMOSPHERIC DYNAMICS

SUBPHOTOSPHERIC CONVECTION

ROBERT F. STEIN

*Physics and Astronomy Department, Michigan State University,
East Lansing, MI 48824, U.S.A.*

and

ÅKE NORDLUND

Copenhagen University Obs., Øster Voldgade 3, Dk-1350 Copenhagen K, Denmark

Abstract. Three-dimensional simulations of solar convection are described. The simulations show that viewing convection as a hierarchy of eddies does not properly represent the large scale topology. A better picture is to view convection as a broad warm upflow with embedded cool, narrow, downdrafts. These downdrafts penetrate many scale heights through the convection zone and carry most of the net convective flux. Near the solar surface there are extremely large fluctuations in the temperature (5000–11000 K), entropy and pressure (factor of four). Radiation temperature does not provide an accurate measure of the gas temperature at a given geometric depth, because the opacity is very temperature sensitive. The emergent intensity in the infrared is smaller and has a smaller contrast than in the visible. However, in terms of radiation temperature the infrared is hotter and has a higher contrast than the visible.

Key words: convection – infrared: stars – Sun: granulation – Sun: interior

1. The Simulation

We simulate the upper portion of the solar convection zone by solving the equations of mass, momentum and energy conservation. The equation of state includes the effects of ionization and excitation of hydrogen, helium and other abundant elements. Three-dimensional radiative transfer at the surface is included assuming LTE and using a 4-bin opacity distribution function. The boundary conditions at the top and bottom are transmitting and in the horizontal directions are taken to be periodic (Nordlund and Stein 1990, Nordlund 1982). We have made two simulations: They both have the upper boundary at the temperature minimum, about 4 pressure scale heights above the top of the convection zone. One extends down about 2.5 Mm and covers a range of about 6 pressure scale heights in the convection zone. The other extends down 9 Mm and covers a range of 10 pressure scale heights through the convection zone.

The mean (horizontally and temporally averaged) atmosphere in these simulations is shown in Figure 1. We first present the topology of the convective flow, then the relation between the flow and the thermodynamic variables. Next we discuss the energetics and finally describe what can be observed.

2. Topology

On a large scale looking at convection as a hierarchy of eddies is not accurate. A better picture is warm, diverging, slow upflows with embedded cool, filamentary, fast downdrafts. Kinetic energy flux isosurfaces (Figure 2) reveal the regions of high velocity. They stop at the visible surface because the velocity decreases rapidly in the photosphere. Long thin downdrafts which penetrate through the entire simulation domain are clearly seen. Another way to visualize the fluid motion is to

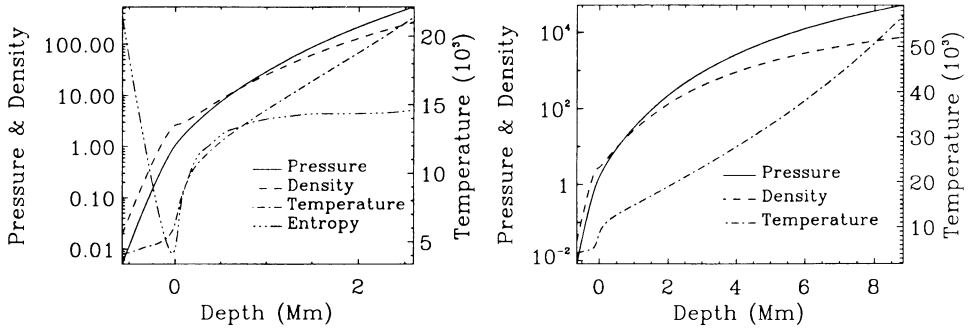


Fig. 1. Mean structure of atmosphere in the numerical simulations. The horizontal and temporal averages are plotted. (a) 2.5 Mm deep atmosphere. (b) 9 Mm deep atmosphere.

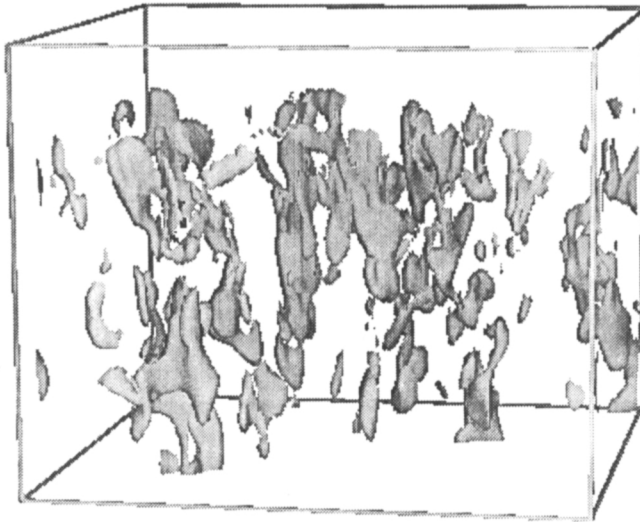


Fig. 2. Kinetic energy flux isosurfaces. The flux level shown is $10^{10} \text{ ergs cm}^{-2} \text{ s}^{-1}$

follow fluid parcels in time. Figure 3 shows fluid parcels which are moving upward through the visible surface at a given time, where they come from and where they move to. These are the fluid parcels that form the centers of the granules. Nine minutes earlier, most of these parcels have come from about the same depth below the surface, but from a much smaller region of the horizontal plane, because the upflow has to diverge in order to conserve mass. Nine minutes later, these fluid parcels are heading downward. They have again concentrated into very small horizontal regions. Downward moving filaments are clearly revealed. They have much larger velocity than the upflow, since in 9 minutes they reach the bottom at 2.5 Mm, whereas in the same amount of time the upflows only moved from about 1 Mm

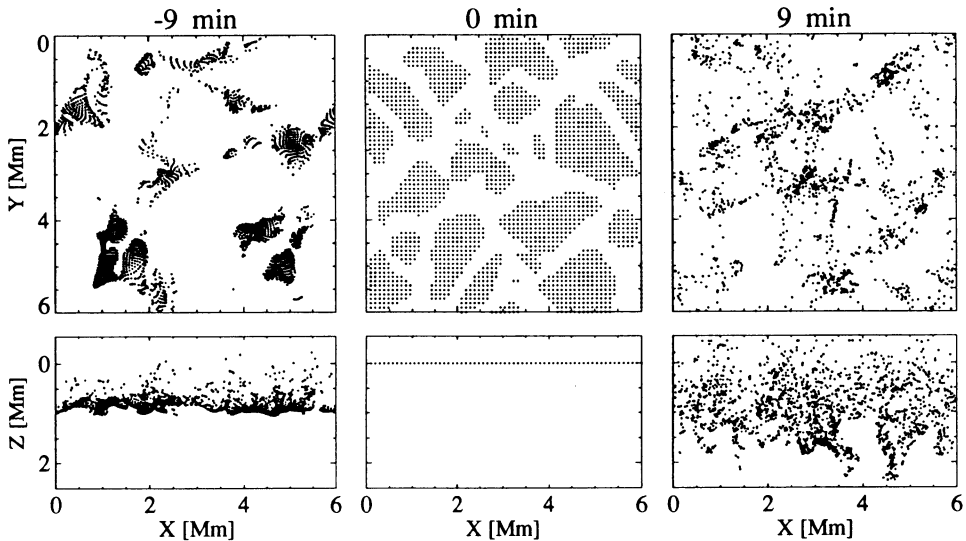


Fig. 3. The origin and destination of fluid parcels ascending through the visible surface at time $t = 0$. Nine minutes earlier, most of these parcels originated from a small source volume – vertically (because they have nearly the same vertical velocity) and horizontally (because the upflow diverges). Nine minutes later, most of the fluid has descended a substantial distance, concentrating into a few filamentary downdrafts.

depth to the surface.

Broad upflows and filamentary downdrafts can also be clearly seen in vertical slices through the simulation domain. Figure 4 shows the velocity in the xz plane and the temperature fluctuation in two such slices from different locations. In Figure 4a, a downdraft extends through the entire depth (10 pressure scale heights). Figure 4b shows two upflows, which diverge and turn over below the surface. Most of the fluid has to turn over before reaching the surface because of mass conservation. Note that the upflow region is very broad compared to the downdraft.

3. Thermodynamics and Flow

Below about 1 Mm the flow is nearly adiabatic. The entropy is nearly constant and its fluctuations are small (Figure 5). At the surface the entropy gradient is superadiabatic and very large. At different locations on the surface this steep jump occurs at slightly different depths ranging from about -50 km, up in the photosphere, to 250 km below the surface. Note that the zero of the height scale lies near the surface, but is arbitrary. $\langle T \rangle = 5800$ K at $z = -30$ km and $\langle \tau_{0.63\mu\text{m}} \rangle = 1$ at $z = -72$ km. There is a very tight correlation between the entropy and the temperature (Figure 6a). Most of the upward moving plasma is hot (11000 K) and most of the cool plasma (6000–7000 K) is moving down (Figure 6b). The hot upflowing plasma has

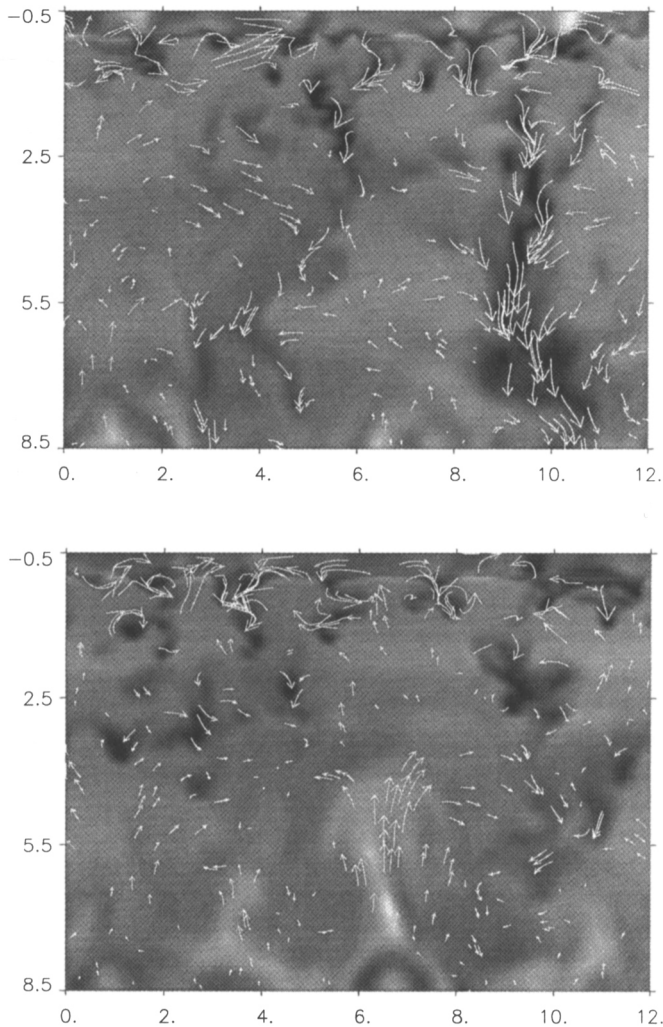


Fig. 4. Velocity and temperature fluctuation ($T - \bar{T}$), scaled by $T_{\max} - T_{\min}$ at each depth, in two vertical slices through the computational domain. Dark is cooler and light is hotter than average. Tick marks indicate horizontal and vertical scale in Mm. The surface is at $z = 0$. (a) Note the filamentary downdraft near the right edge that penetrates through the entire 10 scale heights of the convective region. (b) Note the broad diverging upflows near the center and the left side, with significant overturning several Mm below the surface.

high entropy which gets radiated away when it reaches the surface. Figure 6c shows that this high-entropy, hot, upflowing plasma has low density, while the low entropy, cool, downflowing plasma has higher density. The resulting pressure is fairly constant from point to point at a given depth (Figure 6d).

Near the surface, at a given geometric depth, there is a huge range in tem-

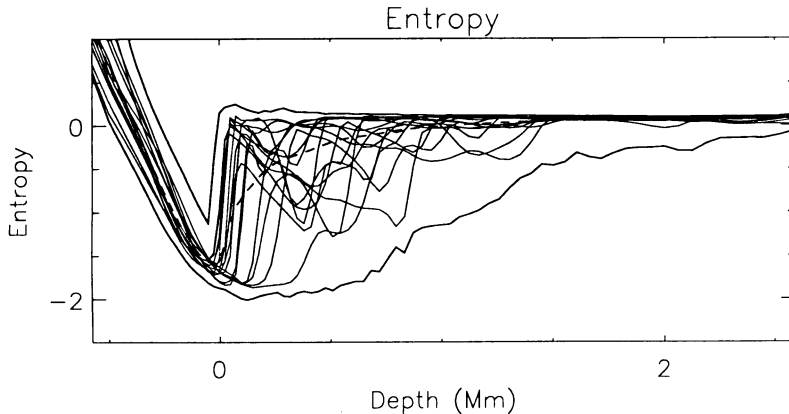


Fig. 5. Entropy as a function of depth is shown for several horizontal locations. Bounding curves are the minimum and maximum entropy. Dashed curve is the mean entropy. Near the surface the entropy gradient is huge and superadiabatic. At depth the entropy becomes nearly uniform.

perature (5000-11000 K) from point to point (Figure 6b). The rms temperature fluctuation is almost 2000 K. In this superadiabatic region the mean temperature gradient peaks at 30 K/km. With increasing depth, the magnitude of the temperature fluctuations decreases rapidly, becoming less than 100 K below 1 Mm.

The rms up, down and horizontal velocities all peak at slightly less than 2 km/sec near the visible surface. The upward rms velocity peaks about 50 km below, the downward rms velocity peaks about 300 km below and the horizontal rms velocity peaks about 100 km above the surface. The downward moving fluid reaches a maximum of about 13 km/s, at 600 km depth where the minimum temperature is 10000 K. The horizontal velocity has maxima of about 10 km/s near the visible surface. Where the horizontal velocity is high in cool intergranular lanes this flow is supersonic and shocks develop. These are nearly vertical standing shocks, like walls around some of the granules.

There is a horizontal cellular structure, of course. Figure 7b shows the temperature distribution at the surface with superimposed horizontal velocities. Note that the regions of high temperature, which are the centers (sometimes the edges) of the granules, are fairly small and the low temperature lanes are quite broad. They are much broader than the intergranular lanes seen in the intensity or the areas of downflow, which correspond closely with the intergranular lanes. Temperature images 50 km further down have larger granules but are still quite different from intensity images. In particular, the hot areas have nearly uniform temperatures and hence appear "burnt out".

Above the surface (Figure 7a), the temperature distribution reverses. Granules become cool due to adiabatic expansion of the diverging upflowing gas in a subadiabatic region, and the intergranular lanes become warm due to adiabatic compression heating. Below the surface (Figure 7c), the hot regions broaden and

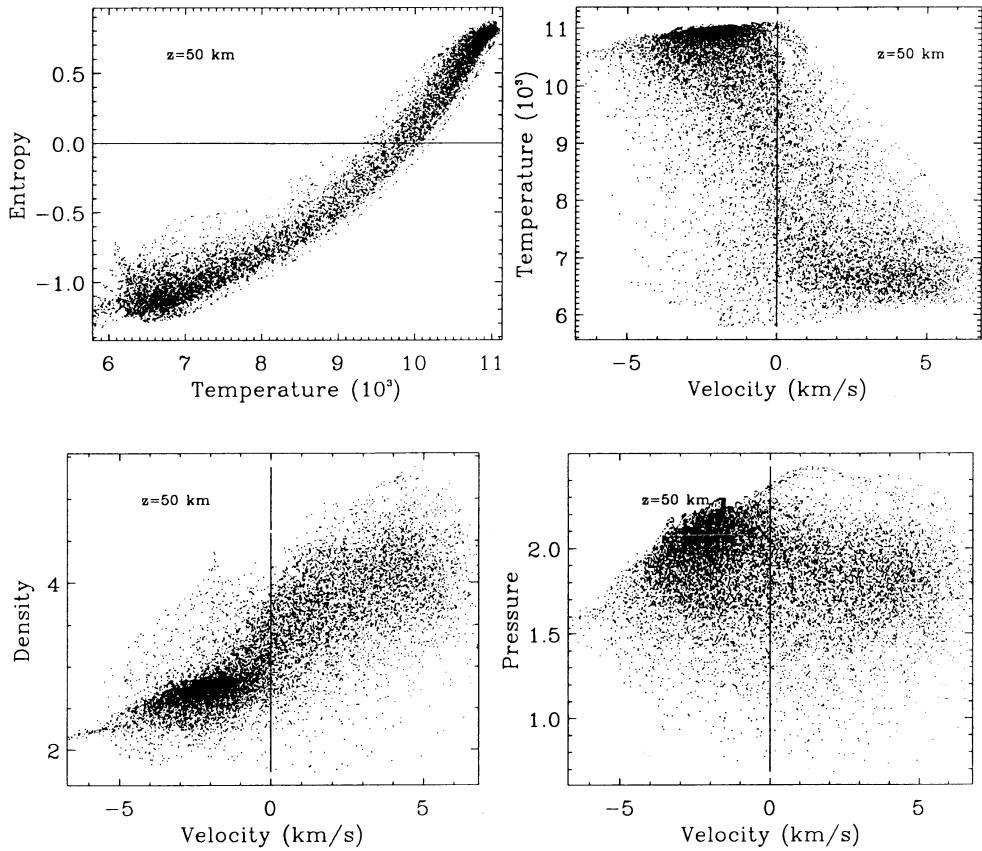


Fig. 6. Atmospheric structure at 50 km depth. Shown are the correlation of entropy with temperature and the correlation of temperature, density and pressure with velocity.

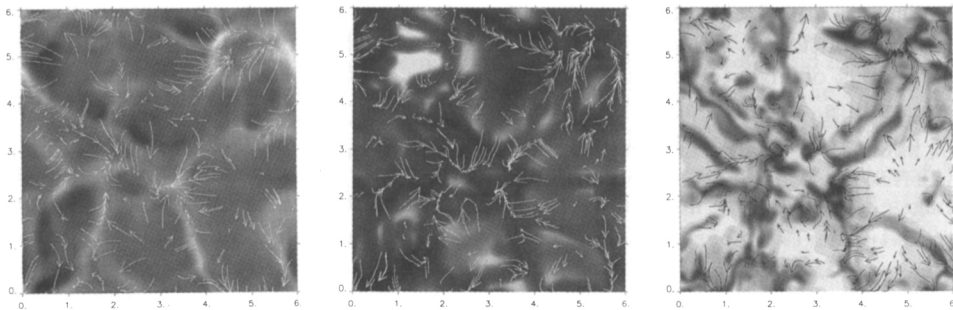


Fig. 7. Temperature and horizontal velocity at (a) -250 km, (b) 0 km (visible surface) and (c) 260 km.

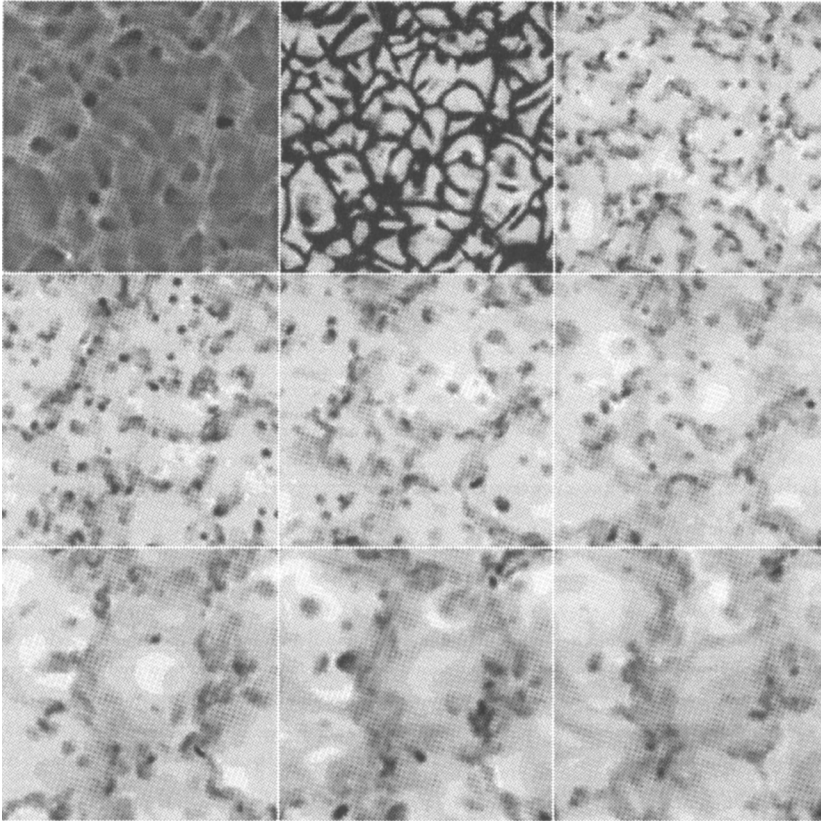


Fig. 8. Temperature on horizontal planes at intervals of 0.5 Mm from -0.5 Mm (temperature minimum) to 3.5 Mm. Light regions are hot and dark areas are cool. Note the increasing size of the hot regions with increasing depth.

the cool intergranular lanes become quite narrow. The flow converges into these cool regions which become the isolated downdrafts. The beginning of this can already be seen at 260 km below the surface. A montage of horizontal slices showing the temperature in steps of 0.5 Mm from -0.5 Mm above the surface to 3.5 Mm below it (Figure 8) shows the cool downdrafts embedded in the hot upflows. Fine scale structure develops a little below the surface. Then the intergranular lanes break up into isolated cool downdrafts in the generally hot upflow. The size of these hot upflow cells increases with depth.

4. Energetics

Above the surface energy is transported outward by the radiative flux, below the surface by the enthalpy (convective) flux (Figure 9). In our model, we take the

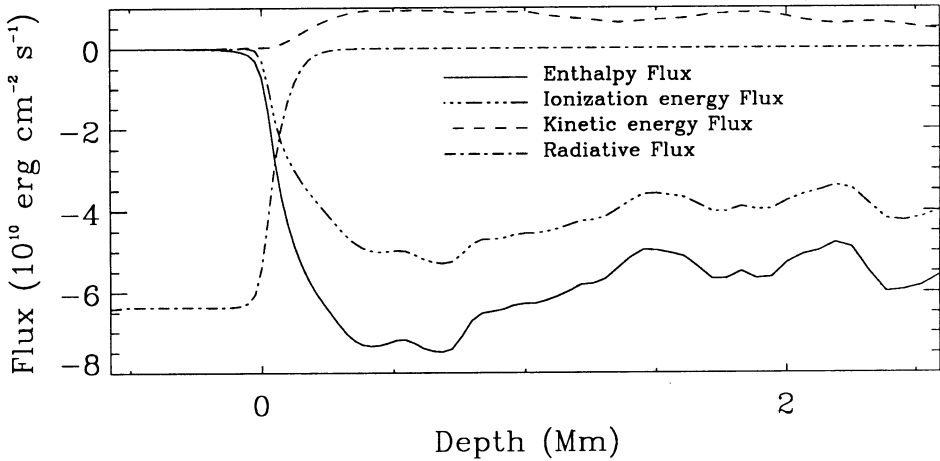


Fig. 9. Radiative, enthalpy (convective), ionization energy (latent heat) and kinetic energy fluxes as a function of depth.

z pointing downward, so upward fluxes are negative. The net upward flux is the sum of the enthalpy flux and the kinetic energy flux, which is always downward. However, the kinetic energy flux is always small compared to the enthalpy flux and so has only a minor impact. Note the large contribution to the enthalpy flux made by the latent heat of ionization. About 2/3 of the heat is carried to the surface as ionization energy.

The various contributions to the flux, summed over the surface area ordered by the vertical velocity, is shown in Figure 10, which reveals the contributions of the up and downflowing plasma. Two depths are shown: 50 km and 1 Mm below the surface. For instance, consider the net flux. Near the surface about half the net flux is carried by the upflows and half by the downflows. Down deeper, most of the net flux, about 70%, is carried by the downflows and only 30% is carried by the upflows. Similarly, near the surface about half the buoyancy work is done in the upflows and half in the downflows, while deeper down most (about 70%) of the work is done in the downflows. It is the cool, low entropy plasma which is doing most of the driving of the convective motions in the interior. However, the amount of driving decreases with depth because the entropy fluctuations decrease with depth (Figure 5).

Several other groups have also been making convective simulations (*e.g.*, Chan and Sofia 1986 and Cattaneo *et al.* 1991). They have simulated inefficient convection of an ideal gas with most of the flux carried by conduction and their results are somewhat different. Cattaneo *et al.* find that in their downflows the downward kinetic energy flux nearly cancels the upward enthalpy flux, so that the net flux is carried almost entirely in the upflows. We have run such a case starting from a snapshot provided by Cattaneo and Malagoli, and find that indeed for inefficient convection of an ideal fluid, most of the flux is carried by the upflows. Hence, there is something different in the physics when one uses an equation of state including

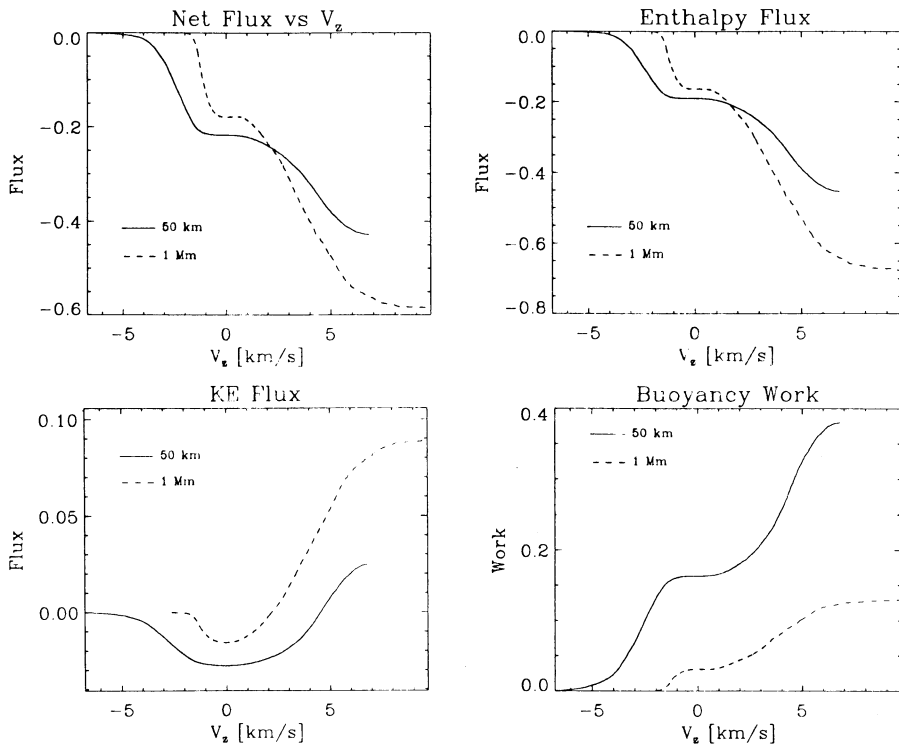


Fig. 10. Net flux, enthalpy flux, kinetic energy flux and buoyancy work at 50 km and 1 Mm depth as a function of fluid velocity. The fluxes and work are summed over area for fluid velocities ranging from maximum upflow to maximum downflow.

ionization and considers a situation of efficient convection.

5. Observables

The emergent intensity generated in the simulation, when smoothed with a point spread function to account for the effects of a telescope and seeing, is very similar to the observed granulation intensity pattern (Figure 11) (see also Lites *et al.* 1989). There are some interesting similarities and differences. In the simulation, many granules are brightest along the edges. Smoothing removes most of these bright edges. The observed image also has granules with bright edges. More recent observations, with exceptional seeing, confirm that granules are often brightest along their edges (Keller and von der Lühe 1992). A comparison of the size spectrum of the simulated and observed granulation is shown in Figure 12. The simulation has less small scale structure, but the large scale structure is reproduced quite well.

We now compare the intensity in the infrared and the visible. To calculate this we used monochromatic Planck functions as the source functions, one at $0.63 \mu\text{m}$ and the other at $1.6 \mu\text{m}$. We used our normal opacity for the $0.63 \mu\text{m}$ calculation

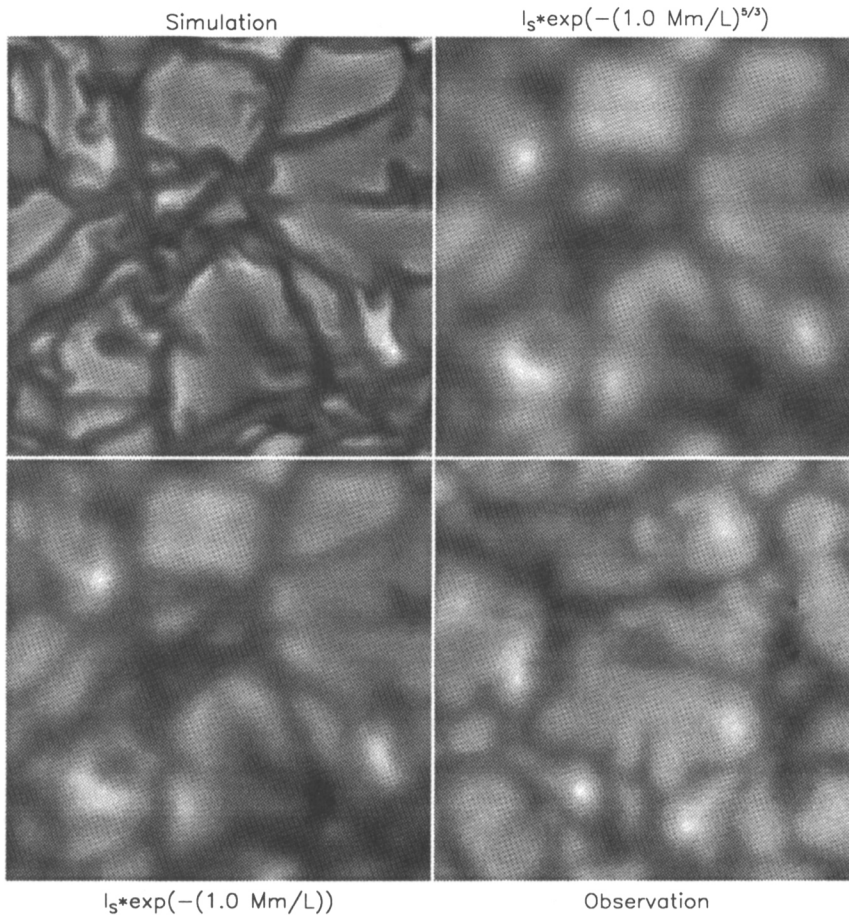


Fig. 11. Comparison of the intensity pattern from the numerical simulation with observations from the Swedish Solar Observatory on La Palma. From left to right and top to bottom the images are (upper left) the emergent intensity from the simulation; (upper right) the same intensity, smoothed with a $\exp(-(k/k_0)^{5/3})$ point spread function representative of a finite instrumental resolution and atmospheric seeing; and (lower left) the same intensity smoothed with an $\exp(-k/k_0)$ point spread function. For both point spread functions $k_0 = 2\pi/1$ Mm. An area of the same size (6×6 Mm) from a slit jaw image obtained at the Swedish Solar Observatory by Bruce Lites is shown at lower right (cf. Lites *et al.* 1989).

and reduced the opacity by a factor of 1.6 for the $1.6 \mu\text{m}$ calculation. Data from Bob Kurucz (private communication) shows that is about the ratio near optical depth one. The emergent intensity at the the two different wavelengths is shown in Figure 13. The two images differ only slightly. Observations at the two wavelengths are likely to differ more for reasons of different seeing and telescope resolution, and

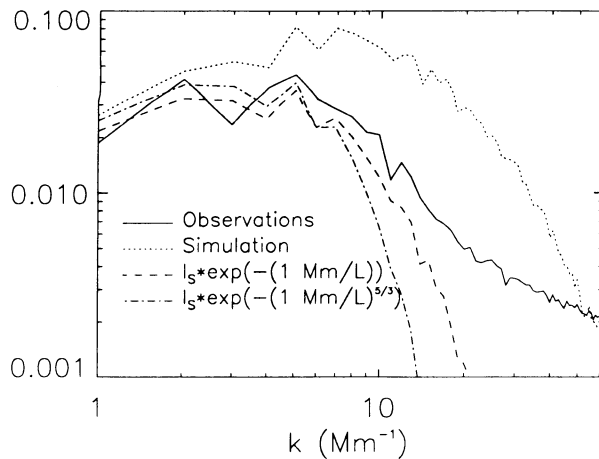


Fig. 12. Horizontal size spectrum of observed and simulated granules including effects of smoothing by two different point spread functions.

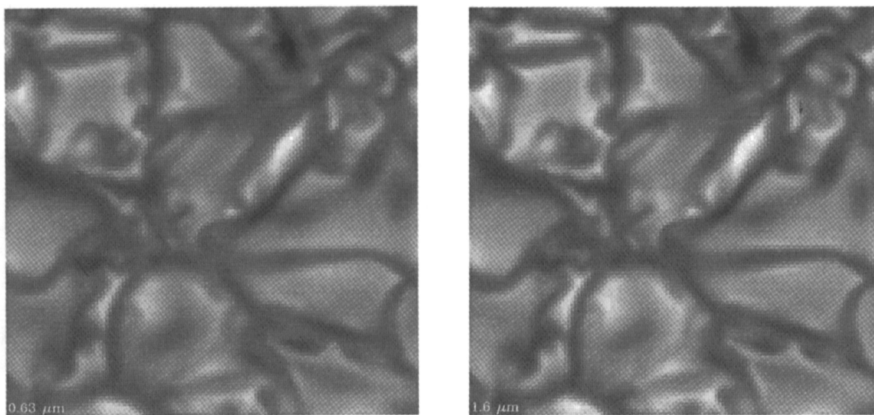


Fig. 13. Emergent intensity at $0.63 \mu\text{m}$ (visible) and $1.6 \mu\text{m}$ (IR) from the same snapshot. Each image is scaled so that its intensity range covers the full grey scale.

have to be of very high quality to reveal true differences. Because of the wavelength dependence of the Planck function, the intensity is smaller and its contrast is less in the infrared compared to the visible. The rms relative intensity fluctuation in the visible is 0.14 and in the infrared is 0.08, so their ratio is 1.7. In terms of the radiation temperature, the infrared is about 300 K hotter and has a 20% greater contrast than the visible (Figure 14).

The radiation temperature (even in LTE) does not correlate well with the gas temperature at a given geometric depth. At $\langle \tau_{1.6\mu\text{m}} \rangle = 1$ the gas temperature varies between 5000 K and 10300 K. The radiation and gas temperatures are well correlated in the cool regions, but the radiation temperature exhibits a much smaller

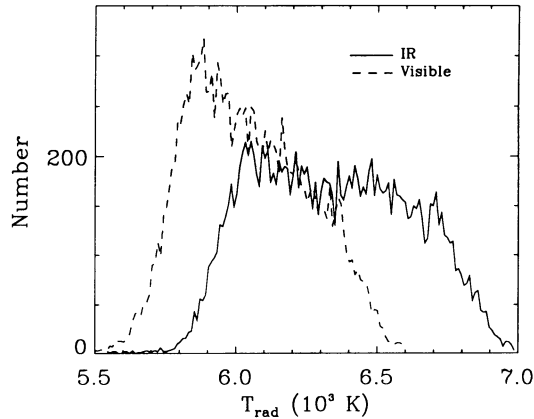


Fig. 14. Histogram of the radiation temperature at 0.63 and 1.6 μm . The average radiation temperature is 6047 K at 0.63 μm and 6352 K at 1.6 μm . The rms relative radiation temperature fluctuation is 0.036 at 0.63 μm and 0.043 at 1.6 μm .

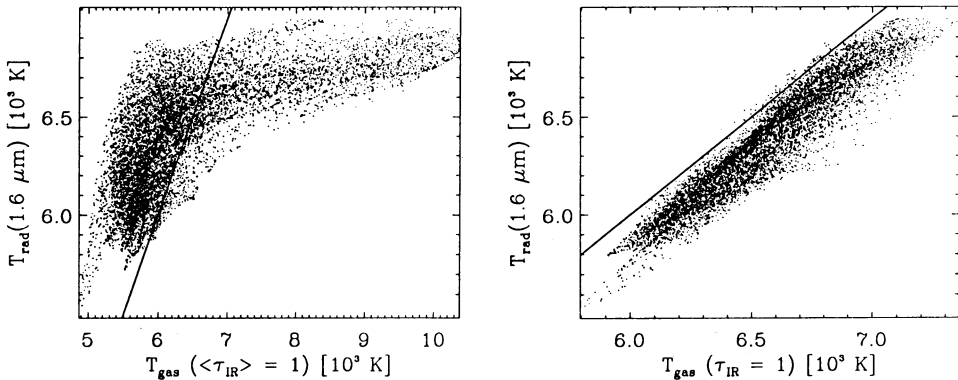


Fig. 15. a) Correlation of radiation temperature at 1.6 μm with gas temperature at depth where $\langle\tau_{1.6\mu\text{m}}\rangle = 1$. b) Correlation of radiation temperature with temperature at the depth where $\tau_{1.6\mu\text{m}} = 1$ locally.

range than the gas temperature (Figure 15a). This is a result of the very rapid increase in opacity with temperature, so one looks into shallower depths in hotter regions and doesn't see the very high temperature gas. In accordance with the Eddington-Barbier relations, the radiation temperature is approximately equal to the gas temperature at optical depth one (Figure 15b). The geometrical height where this occurs varies from place to place and has an rms excursion of 34 km.

Acknowledgements

This work was supported in part by NASA grant NAGW-1695 (RFS) and the Danish Natural Science Research Council and the Danish Space Board (ÅN). The calculations were performed on the Michigan State University Convex 240 and the National Center for Supercomputing Applications Cray 2. The authors appreciate the support of these organizations.

References

- Cattaneo, F., Brummell, N. H., Toomre, J., Malagoli, A. and Hurlburt, N. E.: 1991 *Astrophys. J.* **370**, 282.
- Chan, K. L. and Sofia, S.: 1986 *Astrophys. J.* **307**, 222.
- Keller, C. U. and von der Lühe, O.: 1992, in J. M. Beckers and F. Merkle (eds.), *High Resolution Imaging by Interferometry II*, ESO Conference, in press.
- Lites, B. W., Nordlund, Å. and Scharmer, G. B.: 1989 in R. J. Rutten and G. Severino (eds.), *Solar and Stellar Granulation*, NATO ASI Series **263**, Kluwer Academic Publishers, Dordrecht, pp. 381-399.
- Nordlund, Å.: 1982, *Astron. Astrophys.* **107**, 1.
- Nordlund, Å. and Stein, R. F.: 1990, *Comp. Phys. Comm.* **59**, 119.